AFRL-AFOSR-UK-TR-2020-0017

Constitutive modelling of CMCs for non-proportional, multi-axial loadings

Emmanuel Baranger
ECOLE NORMALE SUPERIEURE
61 AVENUE DU PRESIDENT WILSON
CACHAN, 94230
FR

06/03/2020
Final Report

Air Force Research Laboratory
Air Force Office of Scientific Research
European Office of Aerospace Research and Development
Unit 4515 Box 14, APO AE 09421

REPORT DOCUMENTATION PAGE

Form Approved
OMB No. 0704-0188

1. REPORT DATE *(DD-MM-YYYY)*	2. REPORT TYPE	3. DATES COVERED *(From - To)*
03-06-2020	Final	15 Jun 2018 to 14 Jun 2019

4. TITLE AND SUBTITLE
Constitutive modelling of CMCs for non-proportional, multi-axial loadings

5a. CONTRACT NUMBER

5b. GRANT NUMBER
FA9550-18-1-0432

5c. PROGRAM ELEMENT NUMBER
61102F

6. AUTHOR(S)
Emmanuel Baranger

5d. PROJECT NUMBER

5e. TASK NUMBER

5f. WORK UNIT NUMBER

7. PERFORMING ORGANIZATION NAME(S) AND ADDRESS(ES)
ECOLE NORMALE SUPERIEURE
61 AVENUE DU PRESIDENT WILSON
CACHAN, 94230 FR

8. PERFORMING ORGANIZATION REPORT NUMBER

9. SPONSORING/MONITORING AGENCY NAME(S) AND ADDRESS(ES)
EOARD
Unit 4515
APO AE 09421-4515

10. SPONSOR/MONITOR'S ACRONYM(S)
AFRL/AFOSR IOE

11. SPONSOR/MONITOR'S REPORT NUMBER(S)
AFRL-AFOSR-UK-TR-2020-0017

12. DISTRIBUTION/AVAILABILITY STATEMENT
A DISTRIBUTION UNLIMITED: PB Public Release

13. SUPPLEMENTARY NOTES

14. ABSTRACT
The aim of this study was to explore the possibility of identifying a mechanical non-linear constitutive law from experimental data obtained on oxide/oxide composite tubes presenting an involute meso-structure. For that, a damage model previously developed for ceramic matrix composites was presupposed. For simple loading cases, the model describes correctly the experimental results. For some shear components, the available data was not sufficient. Regarding multi-axial loadings (tension-torsion), the available experimental information didn't allow a robust identification. This work has shown that the proposed model may be adapted to represent experimental results obtained from oxide/oxide composites. Due to the involute meso-structure of the different coupons, the use of a model is necessary to clearly understand the role of the different loading conditions. Before going further with the model, it seems that the experimental results show a rather large scattering in the obtained values. Further work should be conducted to give more robustness to these tests. It should resolve the doubts one can have on the proposed evolutions laws for tension-torsion loadings. Other modeling perspectives are related to the implementation of the model and the description of macroscopic rupture. In the model, there are two origins for failure: 1. fibers reach their capacity to carry the load, as in the case for pure tension; 2. an unstable mechanism develops, as is the case for shear loadings. The first origin can be easily described by a criterion while the second is already introduced in the model via the evolution laws.

15. SUBJECT TERMS
EOARD, ceramic matrix composites, CMC, multi-axial, damage mechanics, modeling, fracture, crack growth

16. SECURITY CLASSIFICATION OF:			17. LIMITATION OF ABSTRACT	18. NUMBER OF PAGES	19a. NAME OF RESPONSIBLE PERSON
a. REPORT	b. ABSTRACT	c. THIS PAGE			GARNER, DAVID
Unclassified	Unclassified	Unclassified	SAR		19b. TELEPHONE NUMBER *(Include area code)* 011-44-1895-616021

Modeling and identification of the mechanical behavior of Ox/Ox composites with involute meso-structure

-

Grant FA9550-18-1-0432 -Constitutive modelling of CMCs for non-proportional, multi-axial loadings

Emmanuel Baranger
LMT, ENS Paris-Saclay, Université Paris-Saclay
94235 Cachan Cedex, France

Period: June 15th 2018 - June 14th 2019

Contents

List of Figures

List of Tables

Summary

The aim of this study is to check the possibility of identifying a mechanical non-linear constitutive law from experimental data obtained on oxide/oxide composite tubes presenting an involute meso-structure. For that, a damage model previously developed for ceramic matrix composites is presupposed. For simple loading cases, the model describes correctly the experimental results. For some shear components, the available data are not sufficient. Regarding multi-axial loadings(tension-torsion), the available experimental information doesn't allow a robust identification.

1 Introduction

Ceramic matrix composites are good candidates for high temperature applications such as civil aircraft engines due to their good specific properties at high temperature under oxidizing environment. Among them, oxide/oxide made of alumina are generally cheaper solutions to produced than SiC CVI materials. The material studied in this paper is a Nextel 720/AS oxide-oxide CMC with an upper temperature limit of 1100^oC as mentioned in DeRienzo (2013). In order to produce tubes for multi-axial testing, the meso-structure of this eight-harness satin weave is organized in an involute layup. This particular layup is presented on Figure 1.

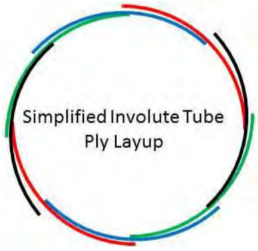

Figure 1: Description of a simplified involute layup on a tube from DeRienzo (2013)

Previous experimental studies have been conducted on this material to characterize its mechanical behavior. Among them, this paper will focus on Hilburn (2014) and DeRienzo (2013). During these two studies, at ambient temperature, planar as well as tubular specimen have been tested. In order to keep the involute meso-structure which is important to form tubes, planar specimen have also been designed to present this particular meso-structure as it will be shown later. The aim of this paper is to check the possibility of identifying a constitutive multi-axial model from such experimental data.

For that, a model has to be chosen. An overview of the different classes of mechanical models of the literature can be found in Baranger (2018) for

ceramic matrix composites. Note that oxide/oxide composites present a rather simple behavior in comparison to SiC/SiC composites. At ambient temperature, mainly cracking occurs and thus most of the models developed use damage mechanics (Lemaitre and Chaboche (1994)) which is macroscopically related to a loss of apparent stiffness. The model used in this paper is related to the work of Ladeveze and LeDantec (1992) on carbon/epoxy UD laminates. This type of model has then be applied to C/C composites by Siron et al. (1999), to SiC/SiC composites by Burr et al. (1995) and Gasser et al. (1998). It has been extended to carbon/epoxy fabrics by Hochard et al. (2001). A similar theory has been developed to describe the compliance evolution of C/C by Camus (2000). Of course other model exists, for example Zok uses Genin and Hutchinson (1997) and Sally et al. (2018) uses the model developed at ONERA.

In this paper, the chosen model will be first described and then identified step by step starting from tests on planar coupons and then from tubular coupons.

2 Methods, assumptions and procedures

2.1 Notations, and general assumptions

The axes related to the local material orientations are :

- In-plane longitudinal direction: $\underline{e}_1$
- In-plane transverse direction: $\underline{e}_2$
- Out-of-plane direction: $\underline{e}_3$

α is the involute angle, about 7 degrees. The reinforcement is an eight-harness satin weave that is supposed to lead to equivalent longitudinal and transverse properties. On top of this, a systematic [0/90]-like layup has been used in the experimental work. Note that $c = \cos\alpha \approx 0.99$ and $s = \sin\alpha \approx 0.12$.

The material of the different coupons is supposed to be homogeneous and orthotropic at the ply scale. Classical beam formulas are used to extract local data at the ply scale from experiments. It is assumed that the kinematics imposed by the grips on the tested coupons impose only very limited edge effects. This effect is introduced by the involute angle in the out of plane direction.

2.2 Proposed constitutive state laws

In the following, the longitudinal and transverse moduli are assumed to be equal, $E_1^0 = E_2^0$ as well as $G_{13}^0 = G_{23}^0$, due to the structure of the involute laminate. Unilateral contact in micro-cracks is not taken into account and only damage is modeled for the moment. The strain energy density $\rho\Psi$ is assumed to read (σ

is the stress tensor):

$$\begin{aligned}\rho\Psi = &+ \frac{1}{2}\frac{\sigma_{11}^2}{E_1^0(1-d_1)} + \frac{1}{2}\frac{\sigma_{22}^2}{E_2^0(1-d_2)} + \frac{1}{2}\frac{\sigma_{33}^2}{E_3^0(1-d_3)} \\ &- \frac{\nu_{12}}{E_1^0}\sigma_{11}\sigma_{22} - \frac{\nu_{13}}{E_1^0}\sigma_{11}\sigma_{33} - \frac{\nu_{23}}{E_1^0}\sigma_{22}\sigma_{33} \\ &+ \frac{1}{2}\frac{\sigma_{12}^2}{2G_{12}^0(1-d_{12})} + \frac{1}{2}\frac{\sigma_{13}^2}{2G_{13}^0(1-d_{13})} + \frac{1}{2}\frac{\sigma_{23}^2}{2G_{23}^0(1-d_{23})} \end{aligned} \tag{1}$$

The term including Poisson's coefficients ν_{ij} are not affected by damage as in the homogenized results obtained from micro-mechanics by Lene and Leguillon (1982). The terms E_i^0 are the initial stiffness moduli while G_{ij}^0 are the initial shear moduli. The thermodynamical forces associated to the damage variables $Y_k = \frac{\partial\rho\Psi}{\partial d_k}|_\sigma$ are:

$$Y_1 = \frac{1}{2}\frac{\sigma_{11}^2}{E_1^0(1-d_1)^2} \tag{2}$$

$$Y_2 = \frac{1}{2}\frac{\sigma_{22}^2}{E_2^0(1-d_2)^2} \tag{3}$$

$$Y_3 = \frac{1}{2}\frac{\sigma_{33}^2}{E_3^0(1-d_3)^2} \tag{4}$$

$$Y_{12} = \frac{1}{2}\frac{\sigma_{12}^2}{2G_{12}^0(1-d_{12})^2} \tag{5}$$

$$Y_{13} = \frac{1}{2}\frac{\sigma_{13}^2}{2G_{13}^0(1-d_{13})^2} \tag{6}$$

$$Y_{23} = \frac{1}{2}\frac{\sigma_{23}^2}{2G_{23}^0(1-d_{23})^2} \tag{7}$$

The identification game is then to describe the evolution of the damage variables $\{d_k\}$ regarding the set of $\{Y_k\}$ via evolution laws. For that, each loading conditions will be described in the local basis to be able to define the values of the thermodynamical forces on one side and the evolution of the stiffnesses (i.e. damage variable evolutions) on the other side. Then, experimental values gives the evolution laws as the relations between these two sets of variables.

3 Results and discussion: coupons from plates

As mentioned in the introduction, some coupons have been extracted from a plate with the involute meso-structure depicted on Figure 2. On this figure, α is the involute angle. The tests conducted by DeRienzo (2013) are used in this section.

In the work of DeRienzo (2013), the axes are named:

- Straight sided: $\underline{e}_X$

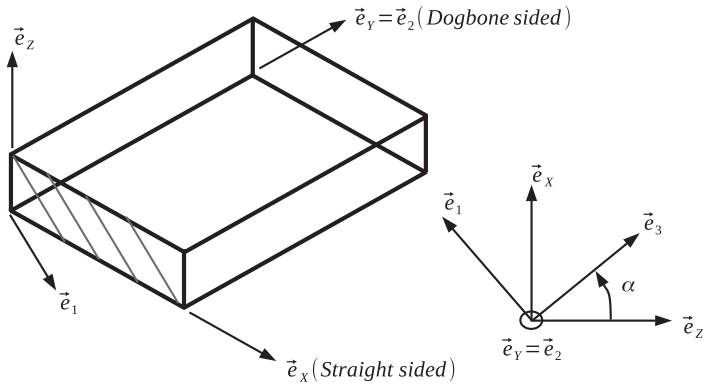

Figure 2: Description of the plate

- Dogbone sided: $\underline{e}_Y$
- Plate thickness: $\underline{e}_Z$

The local material orientation is related to the global basis by:

$$\underline{e}_X = c\,\underline{e}_1 + s\,\underline{e}_3 \tag{8}$$
$$\underline{e}_Y = \underline{e}_2 \tag{9}$$
$$\underline{e}_Z = -s\,\underline{e}_1 + c\,\underline{e}_3 \tag{10}$$

Or

$$\underline{e}_1 = c\,\underline{e}_X - s\,\underline{e}_Z \tag{11}$$
$$\underline{e}_2 = \underline{e}_Y \tag{12}$$
$$\underline{e}_3 = s\,\underline{e}_X + c\,\underline{e}_Z \tag{13}$$

The local stress state is related to the global stress via:

$$\sigma_{11} = c^2\sigma_{XX} + s^2\sigma_{ZZ} - 2cs\sigma_{XZ} \tag{14}$$
$$\sigma_{22} = \sigma_{YY} \tag{15}$$
$$\sigma_{33} = s^2\sigma_{XX} + c^2\sigma_{ZZ} + 2cs\sigma_{XZ} \tag{16}$$
$$\sigma_{12} = c\sigma_{XY} - s\sigma_{YZ} \tag{17}$$
$$\sigma_{13} = cs\sigma_{XX} - cs\sigma_{ZZ} + (c^2 - s^2)\sigma_{XZ} \tag{18}$$
$$\sigma_{23} = s\sigma_{XY} + c\sigma_{YZ} \tag{19}$$

3.1 Loading case: pure tension in direction Y - dogbone sided

The stress state in the coupon reads:

$$\sigma_{22} = \sigma_{YY} \tag{20}$$

$$\sigma_{11} = \sigma_{33} = \sigma_{12} = \sigma_{13} = \sigma_{23} = 0 \tag{21}$$

3.1.1 Coupon 12-110

The stress-strain law is shown on Figure 3. The upper figure presents the raw data in blue and in red the limited zone where the modulus has been identified. The lower figure presents the data with a shift regarding the strains. The modulus is identified to be: $E_2^0 = 67.3GPa$. As no unloading-loading loops have been performed, it is impossible to determine from this data if the nonlinearity is linked to some inelastic strain or to a stiffness loss. It is assumed that everything is due to the stiffness loss i.e. damage.

The associated thermodynamical forces are:

$$Y_2 = \frac{1}{2}\frac{\sigma_{YY}^2}{E_2^0(1-d_2)^2} = \frac{1}{2}E_2^0\varepsilon_{YY}^2 \tag{22}$$

$$Y_1 = Y_3 = Y_{12} = Y_{13} = Y_{23} = 0 \tag{23}$$

The damage evolution law is shown on Figure 4 in blue. It is strongly oscillating because the strain is oscillating. The identification of the damage variable is given by:

$$d_2 = 1 - \frac{E_2}{E_2^0} \; ; \; E_2 = \frac{\sigma_{22}}{\varepsilon_{22}} \tag{24}$$

The fitted law, presented in black, is of the form:

$$d_2 = \max[a\sqrt{Y_2} + b, 0] \tag{25}$$

with $a = 0.39MPa^{-1/2}$ and $b = -0.049$.

3.1.2 Coupon 12-112

The coupon 12-112 have been loaded using loading-unloading cycles as presented on Figure 5. The stress-strain curve is shown on Figure 6. On this Figure, the strain has been shifted to begin at 0. The modulus is identified by fitting the first cycle: $E_2^0 = 79.6GPa$. It is very different from the first coupon as shown on Figure 7.

From each cycle, a straight line is fitted to extract the evolution of the modulus and inelastic strain. Each value is associated to the maximum loading applied to the coupon before the unloading cycle. The evolution of damage and inelastic strain is shown on Figure 8. It can be observed that the inelastic strain is one order of magnitude less than the total strain. Therefore it will

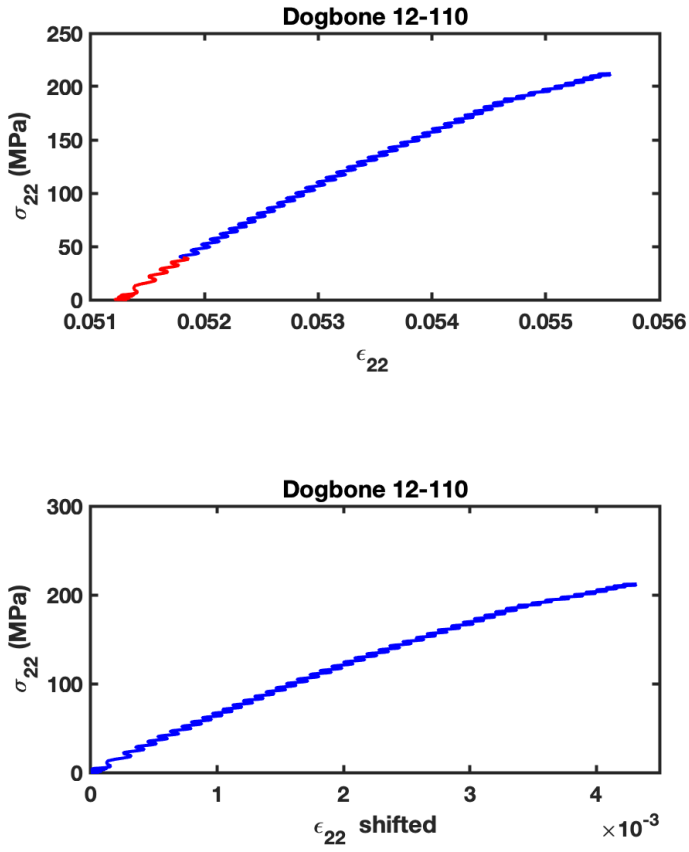

Figure 3: Stress -strain curve for coupon 12-110

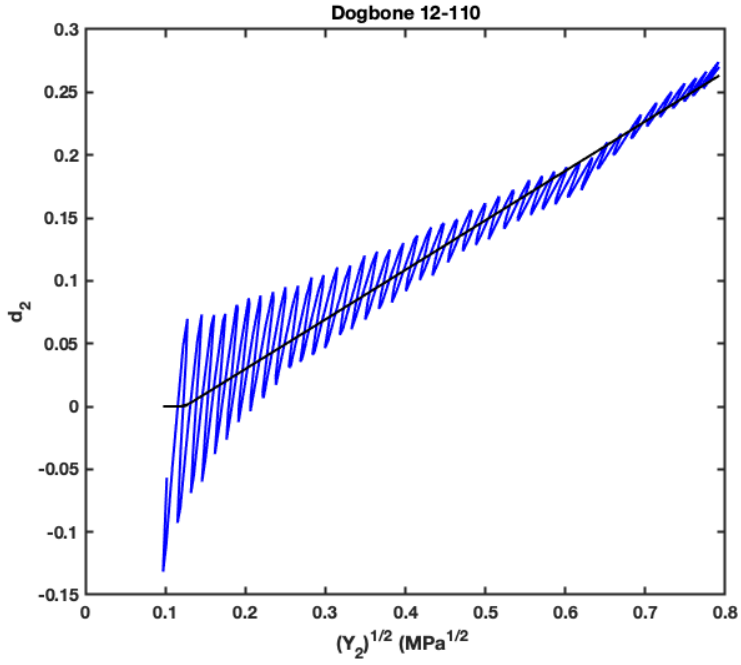

Figure 4: Damage evolution law for coupon 12-110

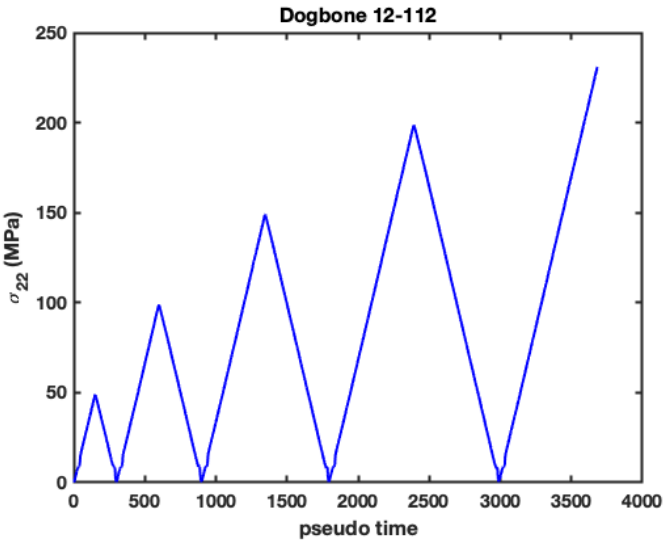

Figure 5: Stress vs. pseudo time curve for coupon 12-112

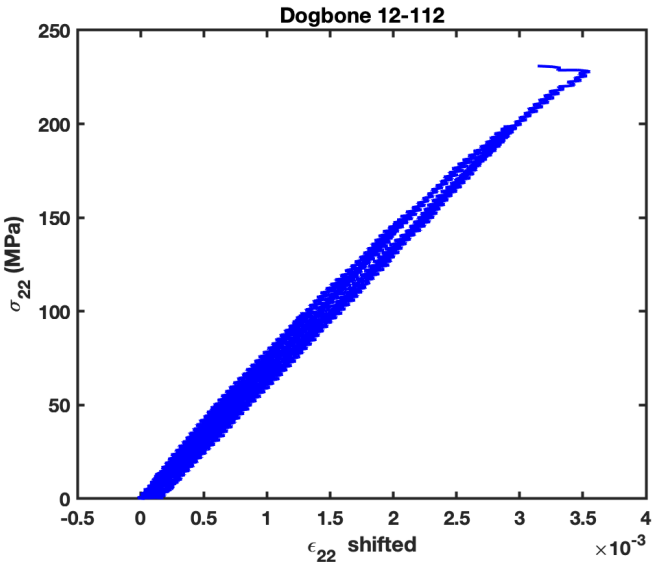

Figure 6: Stress-strain curve for coupon 12-112

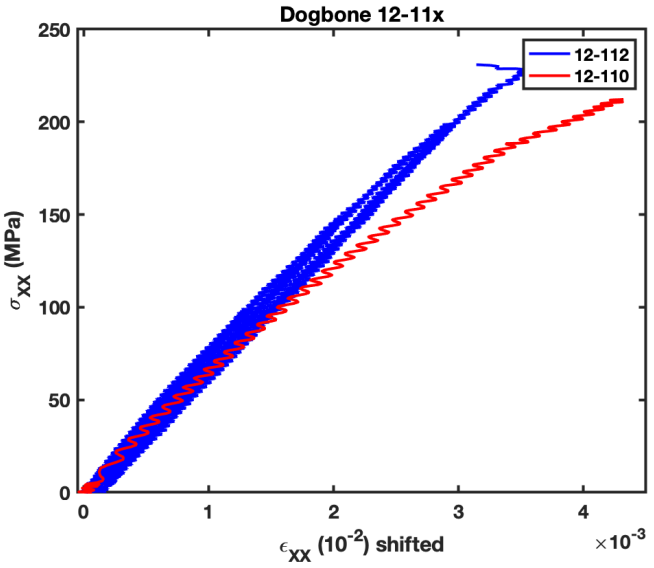

Figure 7: Stress-strain curves for coupon 12-112 and 12-110

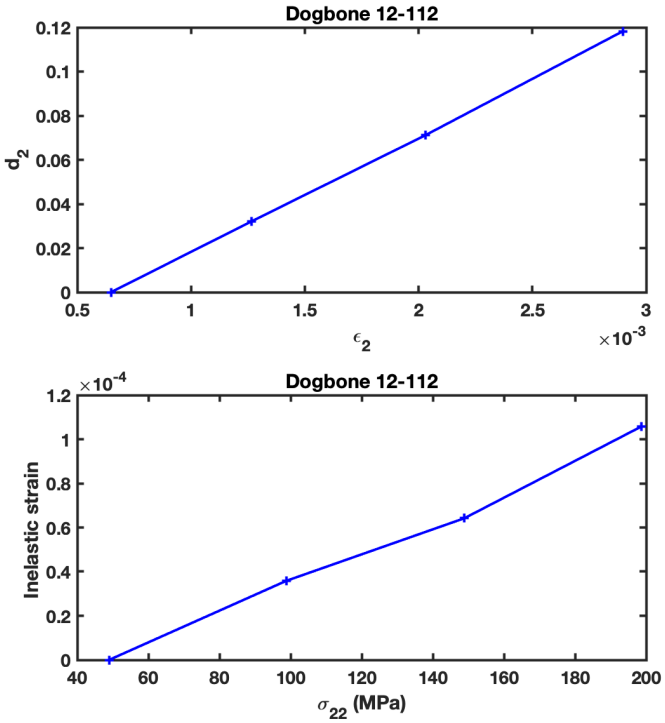

Figure 8: Evolution of the damage and inelastic strain at each cycle for coupon 12-112

be neglected in the following (for other tests without unloading cycles, it is impossible to split the contributions between damage and inelastic strain).

The damage evolution law is shown on Figure 9 in blue. The identification of the damage variable is given by:

$$d_2 = 1 - \frac{E_2}{E_2^0} \tag{26}$$

The fitted law, presented in red, is of the form:

$$d_2 = \max[a\sqrt{Y_2} + b, 0] \tag{27}$$

with $a = 0.23MPa^{-1/2}$ and $b = -0.0344$. There is a very big difference between the two identified laws in this direction as shown on Figure 10.

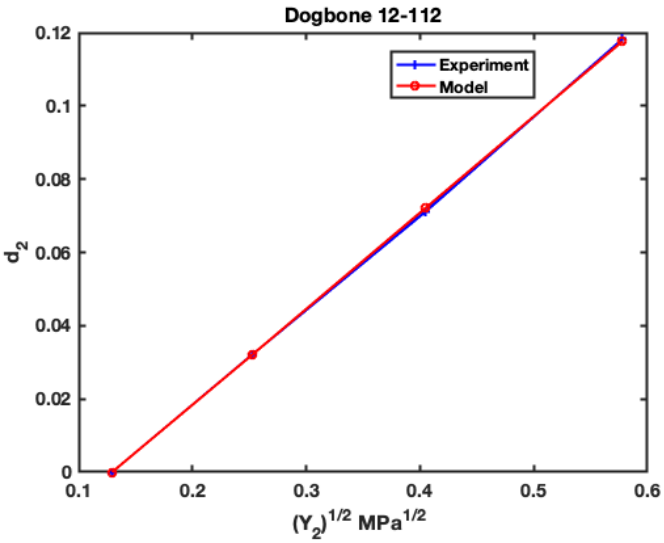

Figure 9: Damage evolution law for coupon 12-112

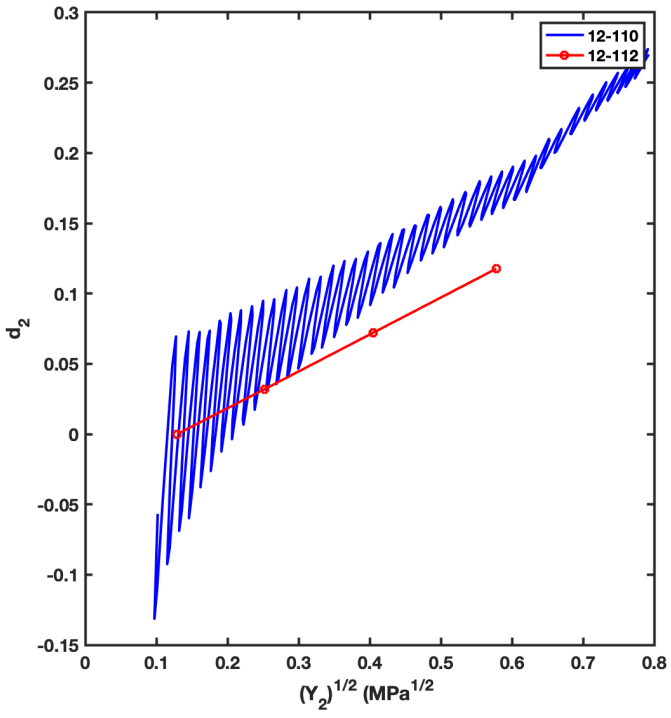

Figure 10: Evolution of the damage evolution laws for two similar coupons 12-110 and 12-112

3.2 Loading case: pure tension in direction X - straight sided

The stress state in the coupon reads:

$$\sigma_{11} = c^2\sigma_{XX} \tag{28}$$
$$\sigma_{33} = s^2\sigma_{XX} \tag{29}$$
$$\sigma_{13} = cs\sigma_{XX} \tag{30}$$
$$\sigma_{22} = \sigma_{12} = \sigma_{23} = 0 \tag{31}$$

Therefore, the preponderant stress is σ_{11} due to the value of s (about 0.1). It is a multi-axial proportional state of stress. The associated thermodynamical forces read:

$$Y_1 = \frac{1}{2}\frac{c^4\sigma_{XX}^2}{E_1^0(1-d_1)^2} \tag{32}$$
$$Y_3 = \frac{1}{2}\frac{s^4\sigma_{XX}^2}{E_3^0(1-d_3)^2} \tag{33}$$
$$Y_{13} = \frac{1}{2}\frac{c^2s^2\sigma_{XX}^2}{2G_{13}^0(1-d_{13})^2} \tag{34}$$
$$Y_2 = Y_{12} = Y_{23} = 0 \tag{35}$$

To compare the order of magnitude of the different thermodynamical forces for damages equal to zero, the following dimensionless forces are introduced (it would be the same for strain energies):

$$\frac{2Y_1E_1^0}{\sigma_{XX}^2} = c^4 \tag{36}$$
$$\frac{2Y_3E_1^0}{\sigma_{XX}^2} = s^4\frac{E_1^0}{E_3^0} \tag{37}$$
$$\frac{2Y_{13}E_1^0}{\sigma_{XX}^2} = c^2s^2\frac{E_1^0}{2G_{13}^0} \tag{38}$$

Two remarks can be done:

- It is supposed that G_{13}^0 and E_3^0 have the same order of magnitude which leads to $Y_{13} >> Y_3$.
- Considering the involute angle value, Y_1 and Y_{13} can have the same order of magnitude if the ratio $\frac{G_{13}^0}{E_1^0}$ is around 1/70 which is certainly not the case here, at least initially. Therefore Y_1 is preponderant.

The strain energy related to E_1^0 is preponderant and thus the constitutive law applied is the one related to the evolution of this modulus and the access to the value of G_{13}^0 won't be possible from this test (same for Y_{13}). However, one may

obtain some clues on failure. In the following, we will remark that the failure is too early if related to d_1. In fact, due to the symmetry assumption, d_1 has to follow the same evolution law as d_2 that has been previously identified.

Keeping the two major terms in the macroscopic strain reads (neglecting the term in E_3^0):

$$\varepsilon_{XX} = \frac{\partial \rho \Psi}{\partial \sigma_{XX}} = \frac{1}{E_1^0}\left(\frac{c^4}{(1-d_1)} + \frac{E_1^0 c^2 s^2}{2G_{13}^0(1-d_{13})}\right)\sigma_{XX} \tag{39}$$

Assuming $c^4 = 0.97 \approx 1$ and $d_1 = 0$, a global damage variable d can be defined as:

$$\varepsilon_{XX} = \frac{1}{E_1^0(1-d)}\sigma_{XX} = \frac{1}{E_1^0}\left(1 + \frac{E_1^0 c^2 s^2}{2G_{13}^0(1-d_{13})}\right)\sigma_{XX} \tag{40}$$

$$\tag{41}$$

Thus, at the first order:

$$d = \frac{E_1^0 c^2 s^2}{2G_{13}^0(1-d_{13})} \tag{42}$$

3.2.1 Coupon 12-098

The stress-strain curve for the coupon 12-098 is shown on Figure 11. The experimental response (with a shifted strain) is compared to a linear model. One can see that the response is almost linear. The modulus is identified $E_1^0 = 67.6GPa$ which close to the value of coupon 12-110, therefore the coefficient $\frac{E_1^0 c^2 s^2}{2G_{13}^0}$ should be neglected. Computing the equivalent damage d variable leads to a very rough profile. The damage evolution law shown on Figure 12 is plotted versus the shear stress (the thermodynamic force is not available as the modulus is not available). A tentative model is given in red. The fitted law, is of the form:

$$d = \max[a\sqrt{\sigma_{13}} + b, 0] \tag{43}$$

with $a = 0.0241MPa^{-1}$ and $b = -0.08$. As G_{13} has not been identified, it is difficult to go back to the identification of the evolution law of d_{13}.

At failure, $d = 0.1$ and thus:

$$0.1 = 0.015\frac{E_1^0}{2G_{13}^0(1-d_{13})} \implies \frac{G_{13}^0}{E_1^0} = 0.075\frac{1}{(1-d_{13})} \tag{44}$$

Assuming a linear evolution law for d_{13} w.r.t ε_{13} (or $\sqrt{Y_{13}}$), an instability occurs for $d_{13} = 0.5$ leading to the theoretical maximum load and thus to failure. This assumption gives:

$$\frac{G_{13}^0}{E_1^0} = 0.15 \tag{45}$$

From this, we conclude that the shear modulus G_{13}^0 would be one order of magnitude less than the longitudinal one E_1^0.

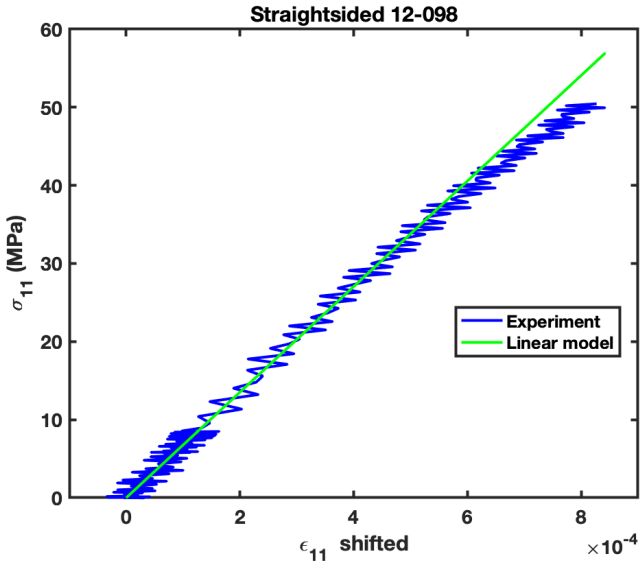

Figure 11: Stress-strain curve for coupon 12-098

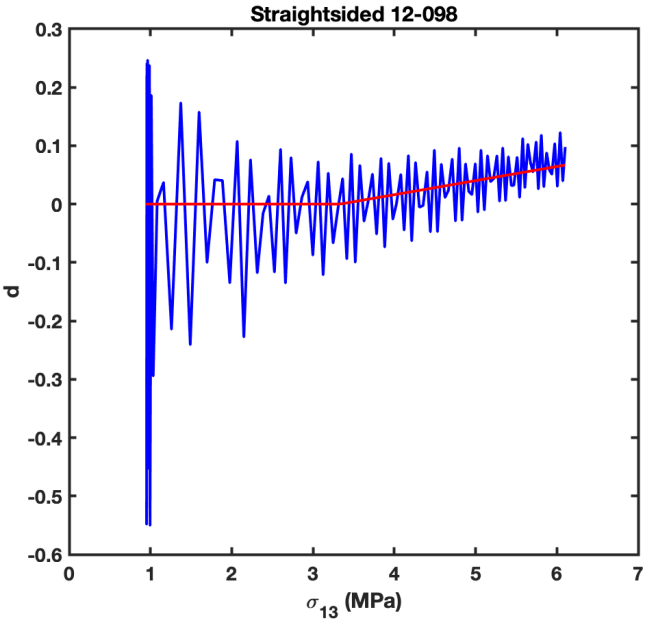

Figure 12: Damage evolution law for coupon 12-098

3.2.2 Coupon 12-106

The stress-strain curve for the coupon 12-106 is shown on Figure 13. The experimental response (with a shifted strain) is compared to a linear model. The modulus is identified $E_1^0 = 59.GPa$ which is below all the values obtained. No damage evolution can be extracted, the maximum shear stress is $4.77MPa$ while it was $6.1MPa$ for the coupon 12-098.

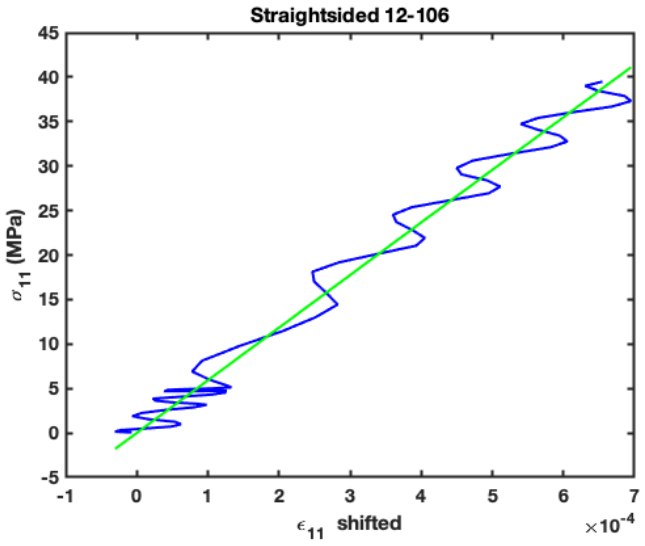

Figure 13: Stress-strain curve for coupon 12-106

4 Results and discussion: coupons from tubes

Some coupons are tubular with the involute meso-structure depicted on Figure 14. On this figure, α is the involute angle. The axes are named:

- Axis of the tube: $\underline{e}_Z$
- Radial axis: $\underline{e}_R$
- Orthoradial axis: $\underline{e}_\theta$

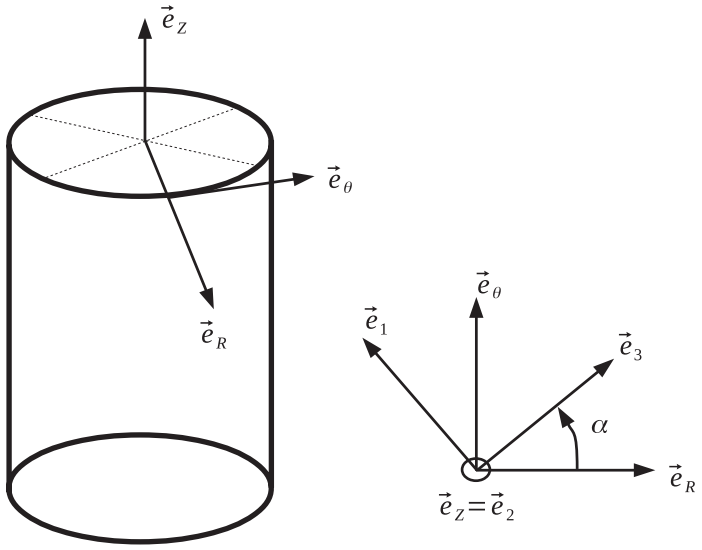

Figure 14: Description of the plate

The local material orientation is related to the global basis by:

$$\underline{e}_R = -s\,\underline{e}_1 + c\,\underline{e}_3 \tag{46}$$
$$\underline{e}_\theta = c\,\underline{e}_1 + s\,\underline{e}_3 \tag{47}$$
$$\underline{e}_Z = \underline{e}_2 \tag{48}$$

Or

$$\underline{e}_1 = -s\,\underline{e}_R + c\,\underline{e}_\theta \tag{49}$$
$$\underline{e}_2 = \underline{e}_Z \tag{50}$$
$$\underline{e}_3 = s\,\underline{e}_\theta + c\,\underline{e}_R \tag{51}$$

The local stress state is related to the global stress state via:

$$\sigma_{11} = s^2\sigma_{RR} + c^2\sigma_{\theta\theta} - 2cs\sigma_{R\theta} \tag{52}$$
$$\sigma_{22} = \sigma_{ZZ} \tag{53}$$
$$\sigma_{33} = c^2\sigma_{RR} + s^2\sigma_{\theta\theta} + 2cs\sigma_{R\theta} \tag{54}$$
$$\sigma_{12} = -s\sigma_{RZ} + c\sigma_{\theta Z} \tag{55}$$
$$\sigma_{13} = -cs\sigma_{RR} + cs\sigma_{\theta\theta} + (c^2 - s^2)\sigma_{R\theta} \tag{56}$$
$$\sigma_{23} = s\sigma_{\theta Z} + c\sigma_{RZ} \tag{57}$$

4.1 Loading case: pure tension in direction Z

There is no experimental data for this case. This loading would lead to the identification of the evolution law of d_2 as for dogbone-sided specimen. It would be interesting to compare results. The stress state in the coupon reads:

$$\sigma_{22} = \sigma_{ZZ} \tag{58}$$
$$\sigma_{11} = \sigma_{33} = \sigma_{12} = \sigma_{13} = \sigma_{23} = 0 \tag{59}$$

$$Y_2 = \frac{1}{2}\frac{\sigma_{ZZ}^2}{E_2^0(1-d_2)^2} \tag{60}$$
$$Y_1 = Y_3 = Y_{12} = Y_{13} = Y_{23} = 0 \tag{61}$$

4.2 Loading case: pure torsion in direction Z

The stress state in the coupon reads:

$$\sigma_{12} = c\sigma_{\theta Z} \tag{62}$$
$$\sigma_{23} = s\sigma_{\theta Z} \tag{63}$$
$$\sigma_{11} = \sigma_{22} = \sigma_{33} = \sigma_{13} = 0 \tag{64}$$

Therefore, the preponderant stress is σ_{12} due to the value of s (about 0.1). The associated thermodynamical forces read:

$$Y_{12} = \frac{1}{2}\frac{c^2\sigma_{\theta Z}^2}{2G_{12}^0(1-d_{12})^2} \approx G_{12}^0\varepsilon_{\theta Z}^2 \tag{65}$$
$$Y_{23} = \frac{1}{2}\frac{s^2\sigma_{\theta Z}^2}{2G_{23}^0(1-d_{23})^2} \tag{66}$$
$$Y_1 = Y_2 = Y_3 = Y_{13} = 0 \tag{67}$$

The comparison of the thermodynamical forces (or of the strain energies) without damage leads to the definition of non-dimension values as:

$$\frac{2Y_{12}2G_{12}^0}{\sigma_{\theta Z}^2} = c^2 \tag{68}$$

$$\frac{2Y_{23}2G_{12}^0}{\sigma_{\theta Z}^2} = s^2\frac{G_{12}^0}{G_{23}^0} \tag{69}$$

Assuming that G_{12}^0 and G_{23}^0 have the same order of magnitude then $Y_{12} >> Y_{23}$ and the macroscopic strain reads:

$$\varepsilon_{\theta Z} = \frac{\partial \rho\Psi}{\partial \sigma_{\theta Z}} = \frac{1}{2G_{12}^0}\left(\frac{c^2}{(1-d_{12})} + \frac{G_{12}^0 s^2}{G_{23}^0(1-d_{23})}\right)\sigma_{\theta Z} \tag{70}$$

$$\approx \frac{1}{2G_{12}^0(1-d_{12})}\sigma_{\theta Z} \tag{71}$$

G_{13} has been estimated to about $0.15E_1^0 = 10GPa$, with the symmetry assumption G_{23} should have the same value. From experimental data and equation 71, the shear modulus 12 will be estimated to $G_{12}^0 = 17GPa$. This validates the initial assumptions on G_{12}^0 and G_{23}^0 having the same order of magnitude.

The stress-strain curve for the coupon 12-063 is shown on Figure 15 for different strain rosettes located on a circumference of the tube ($\gamma_{12} = 2\varepsilon_{12}$). Based on this, the elastic modulus is identified for each measure of strain on the circumference of the tube. $G_{12}^0 = \{17.7; 17.4; 17.9\}GPa$.

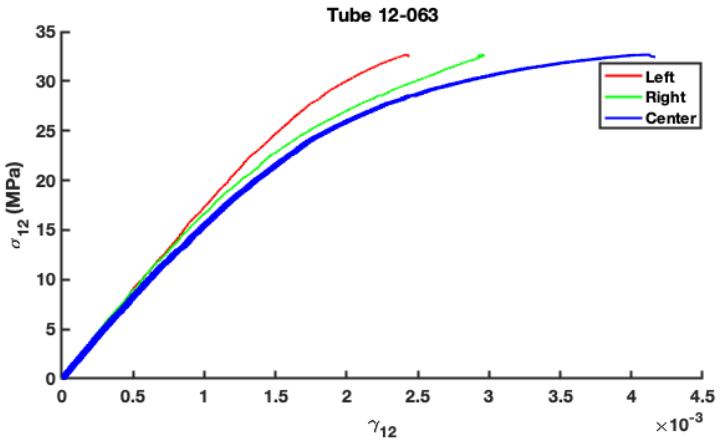

Figure 15: Stress-strain curve for coupon 12-063

The associated damage evolution law is plotted on Figure 16 for the different strain measures. A model, in black, is superimposed. The fitted law, presented in black, is of the form:

$$d_{12} = \max[a\sqrt{Y_{12}} + b, 0] \tag{72}$$

with $a = 2.4MPa^{-1/2}$ and $b = -0.12$. Note that, with this kind of linear law in ε_{12}, a structural instability (strain localization due to a softening behavior) is predicted for $d_{12} = 0.5$. This is consistent with limit values of damage observed as well as the form of the stress-strain curve which exhibits this behavior for the central rosette.

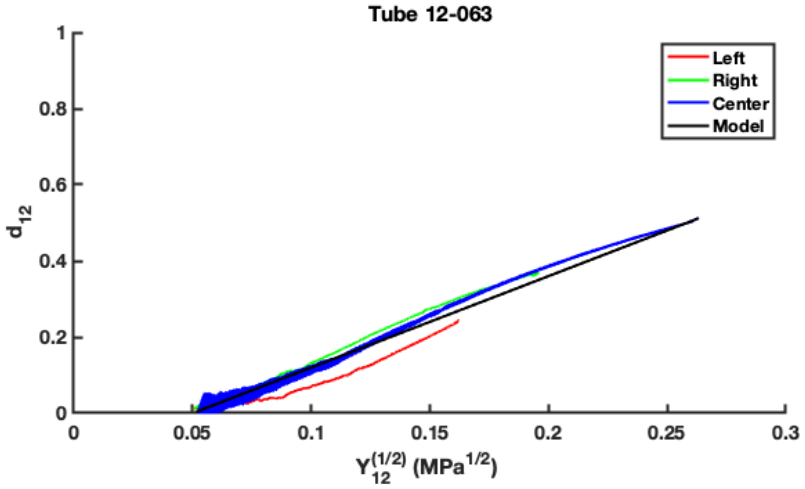

Figure 16: Damage evolution law for coupon 12-063

Note that the maximum stress $\sigma_{\theta Z}$ is about $30MPa$ Therefore $\sigma_{23} = s\sigma_{\theta Z} = 3.6MPa$, just below the maximum shear stress σ_{13} observed on straight-sided coupons. However, due to the scattering observed on other properties, the influence of the associated damage variable remains a question.

4.3 Loading case: combined tension and torsion in direction Z

The stress state in the coupon reads:

$$\sigma_{22} = \sigma_{ZZ} \tag{73}$$
$$\sigma_{12} = c\sigma_{\theta Z} \tag{74}$$
$$\sigma_{23} = s\sigma_{\theta Z} \tag{75}$$
$$\sigma_{11} = \sigma_{33} = \sigma_{13} = 0 \tag{76}$$

The thermodynamical forces read:

$$Y_2 = \frac{1}{2}\frac{\sigma_{ZZ}^2}{E_2^0(1-d_2)^2} \tag{77}$$

$$Y_{12} = \frac{1}{2}\frac{c^2\sigma_{\theta Z}^2}{2G_{12}^0(1-d_{12})^2} \tag{78}$$

$$Y_{23} = \frac{1}{2}\frac{s^2\sigma_{\theta Z}^2}{2G_{23}^0(1-d_{23})^2} \tag{79}$$

$$Y_1 = Y_3 = Y_{13} = 0 \tag{80}$$

4.3.1 Coupon 12-064

First, in the raw experimental files, only the command load and the absolute value of the error have been stored. The loading command is shown on Figure 17. From the error curves, it can be observed that the torque command is difficult to follow. The error being present in the result files, the real loading path is reconstructed and plotted (real loading = command - error). Note that the torque capacity of the load cell is certainly far greater from the needs.

The stress-strain curves are shown on Figure 18 for three different rosettes locations on the same circumference. Stresses and strains have been shifted to start at zero.

To be able to exploit the nonlinear evolution of these curves, initial moduli have been identified as shown on Figure 19. One identification per curve. For the longitudinal modulus it gives $E_2^0 = \{75; 72; 73.6\}GPa$ and for shear $G_{12}^0 = \{14; 12; 13\}GPa$. These data are below the moduli identified from other tests (dog-bone specimen and pure torsion).

Then, the evolution of the damage indicators are extracted as before. Using the evolution laws already identified, each scalar damage variable is related to an equivalent thermodynamical force (named $\bar{Y}_2$ and $\bar{Y}_{12}$) which will depend on the directional thermodynamical forces Y_2 and Y_{12}. The evolutions of the equivalent forces minus the directional forces are shown on Figure 20. These equivalent forces will then be used to drive the damage evolution laws already defined.

It allows to roughly identify a first model as:

$$\bar{Y}_2 = Y_2 + \frac{1}{4}\left(Y_{12}\right)^{1/4} \tag{81}$$

$$\bar{Y}_{12} = Y_{12} + \frac{1}{3}Y_2 \tag{82}$$

Values are not given as the next section will show that too many uncertainties remain on this identification and its understanding.

4.3.2 Coupons A, B and C

Similar tests have been conducted by Hilburn (2014) on tubes for different tension-torsion loading ratios. It seems that a problem occurred with the strain

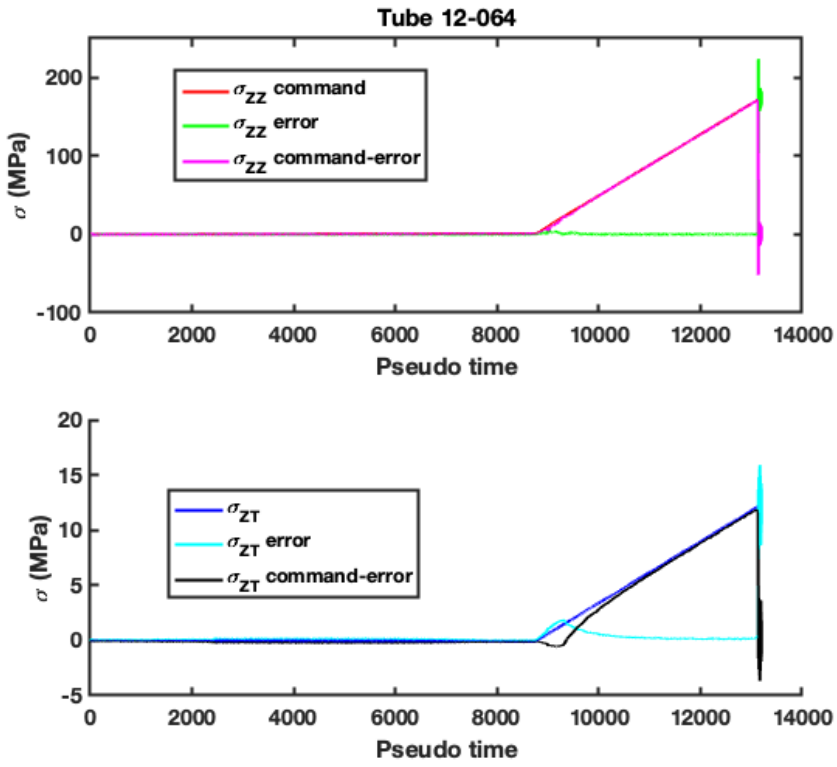

Figure 17: Loading for coupon 12-064

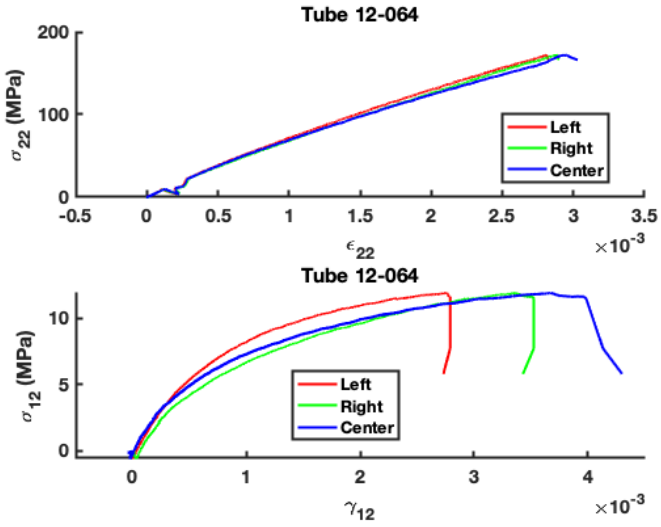

Figure 18: Shifted stress vs. strain curves for coupon 12-064

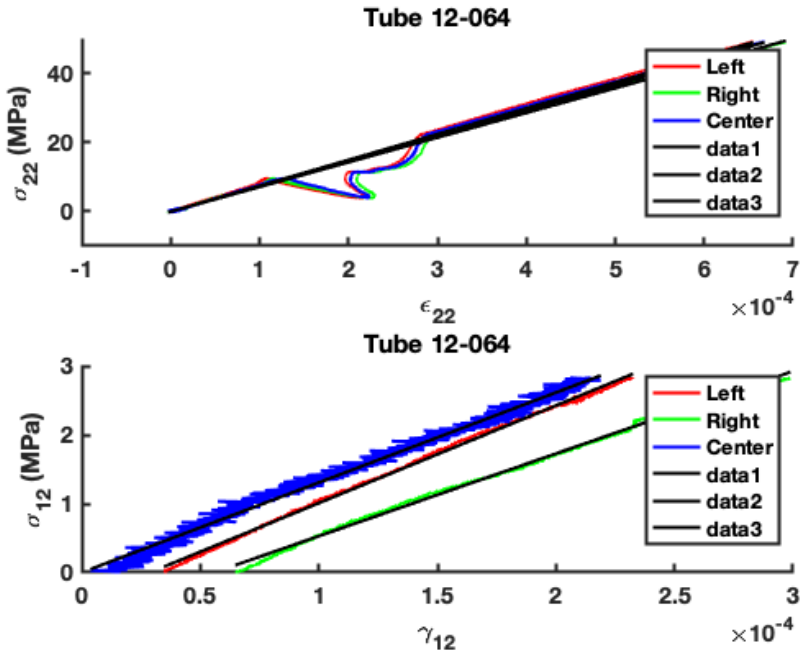

Figure 19: Modulii identification for coupon 12-064

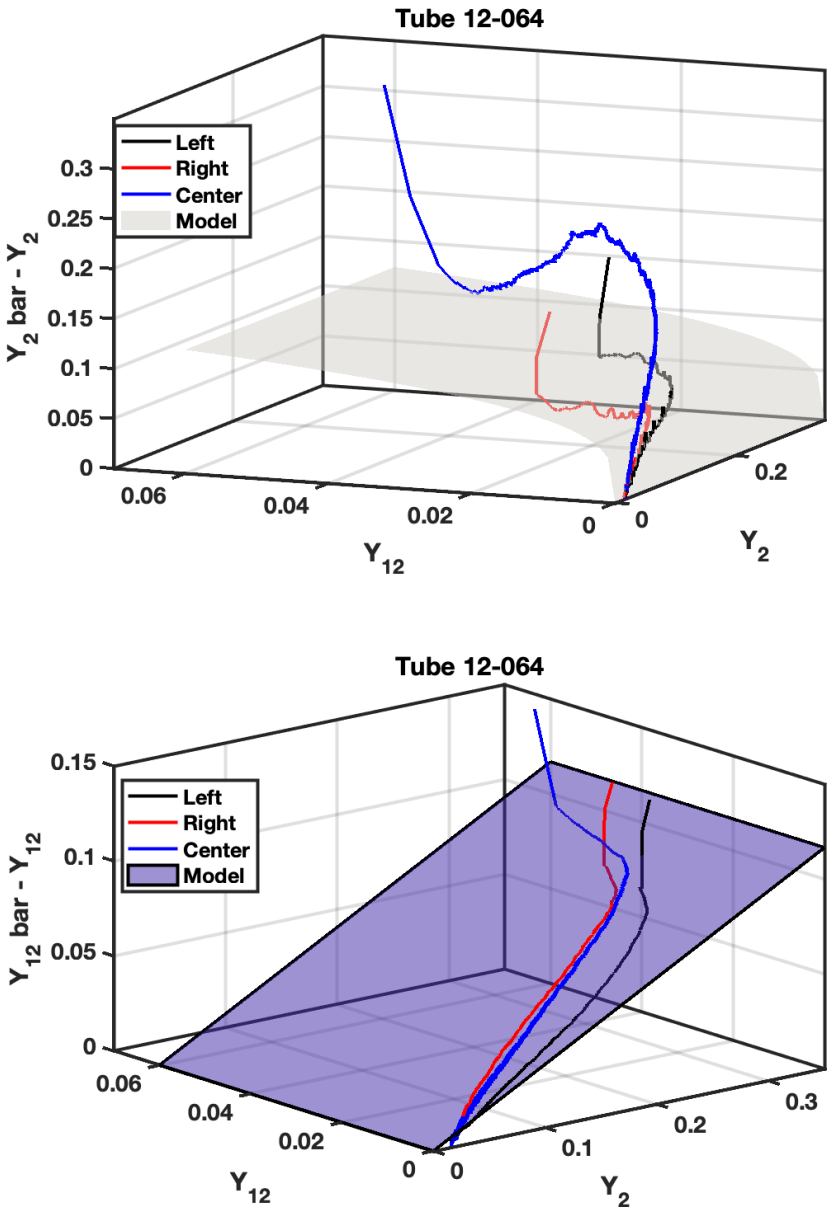

Figure 20: Equivalent thermodynamical forces for coupon 12-064

measurement during these tests as the identified axial and shear moduli are about twice the values identified before. The damage being a quantity which is a relative variation of modulus, it is independent to the measure of strain. It is not the case for the thermodynamical forces and thus the tests have not been fully examined. However, the Figures 21 and 22 show the evolution of $\bar{Y}_2$ and $\bar{Y}_{12}$, post-processed from the damages evaluation and the evolutions laws previously identified, versus the directional thermodynamical forces. These thermodynamical forces don't have the correct values but are proportional to the 'real' forces if the strain measurement error is linear.

For the evolution of $\bar{Y}_2$, the proposed model takes the form $\bar{Y}_2 = c(Y_{12})^{1/4}$ as previously. For the evolution of $\bar{Y}_{12}$, the proposed model takes the form $\bar{Y}_{12} = cY_2^n.Y_{12}^m$ (in the very first attempt proposed $n = m = 1/5$). This form is very unusual and other experiments should be conducted to clarify this point. The same plot is proposed in log scale on Figure 23. The various planes related to the identification conducted in the previous part are shown for illustration. Also note that the shear stress $\sigma_{23} = s\sigma_{\theta Z} = 2.7MPa$ for coupon A and is about $2MPa$ for coupons B and C thus below the failure stress identified earlier. However, due to the scattering observed on other properties, the influence of the associated damage variable remains a question.

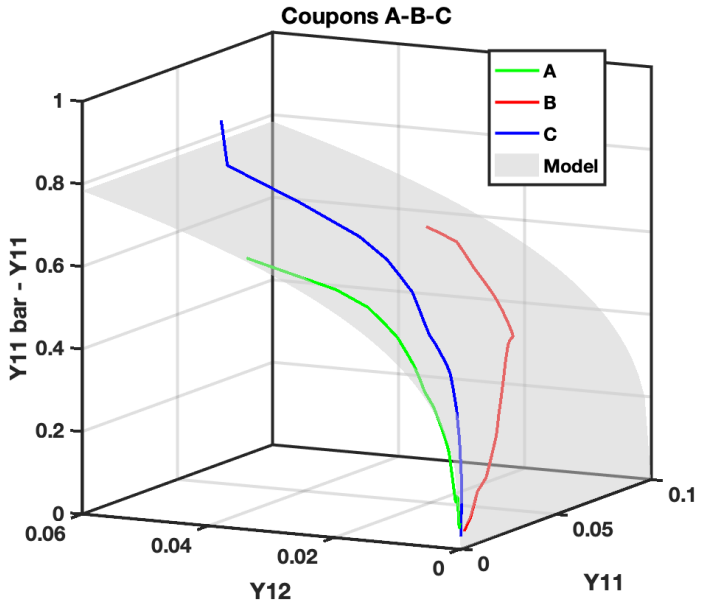

Figure 21: Equivalent thermodynamical force $\bar{Y}_2$ for coupon A-B-C

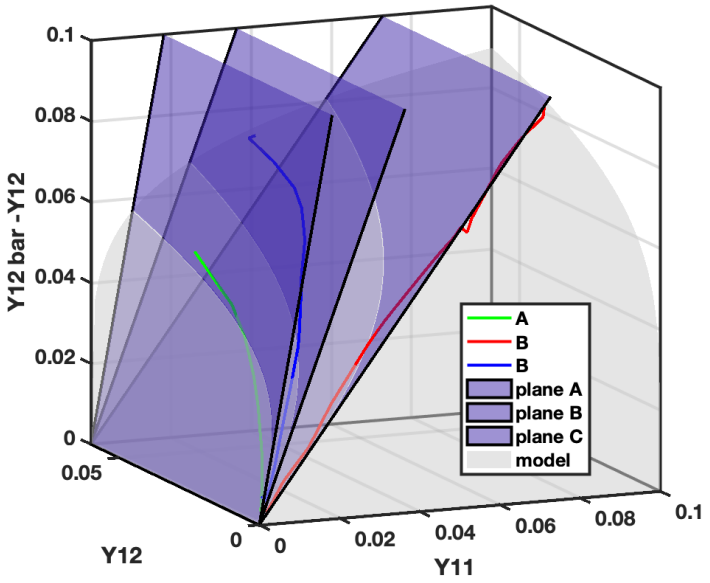

Figure 22: Equivalent thermodynamical force $\bar{Y}_{12}$ for coupon A-B-C

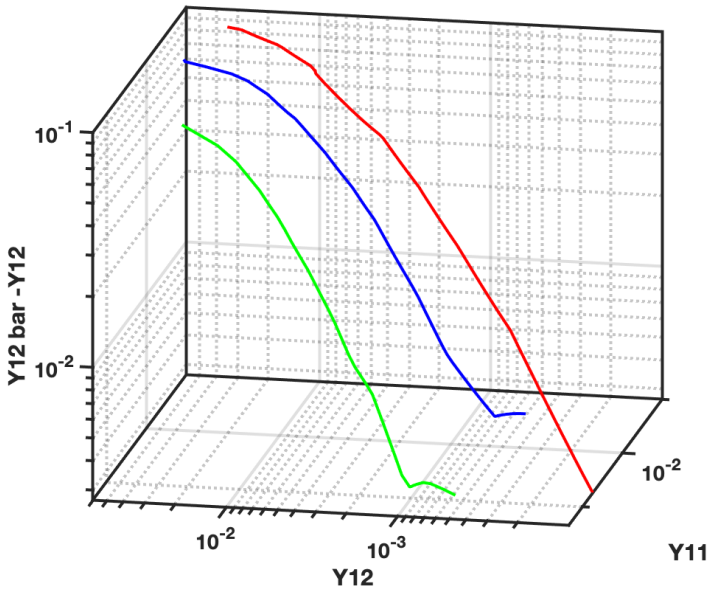

Figure 23: Equivalent thermodynamical force $\bar{Y}_{12}$ for coupon A-B-C

5 Conclusion

This work has shown that the proposed model may be adapted to represent experimental results obtained from oxide/oxide composites. Due to the involute meso-structure of the different coupons, the use of a model is necessary to clearly understand the role of the different loading conditions. Before going further with the model, it seems that the experimental results show a rather large scattering in the obtained values. Further work should be conducted to give more robustness to these tests. It should resolve the doubts one can have on the proposed evolutions laws for tension-torsion loadings. This is the first perspective on the modeling side. Other modeling perspectives are related to the implementation of the model and the description of macroscopic rupture. In the model, there are two origins for failure:

- fibers reach their capacity to carry the load, it is the case for pure tension.
- an unstable mechanism develops, it is the case for shear loadings.

The first origin can be easily described by a criterion while the second is already introduced in the model via the evolution laws. The pic of instability is related to the evolution law (for a linear damage evolution law, it is for $d_k = 0.5$). The main issue related to the management of localization which classically leads to mesh dependencies (see the review from Bazant and Jirásek (2002)) and spurious energy dissipations.

6 List of Symbols, Abbreviations and Acronyms

CMC	Ceramic Matrix Composite
σ, σ_{ij}	Stress, stress component ij
$\varepsilon, \varepsilon_{ij}$	Strain, strain component ij
E_i^0	Initial Young's modulus in the direction $\vec{e}_i$
G_{ij}^0	Initial shear modulus
ν_{ij}	Poisson's coefficients
d_k, Y_k	Damage associated to the k component and th associated thermodynamical force

References

Baranger, E. (2018). Modeling mechanical behavior of ceramic matrix composites. In C. H. Zweben, P. B., editor, *Comprehensive Composite Materials II*, volume 5: Ceramic and Carbon Matrix Composites, pages 237–268. Elsevier.

Bazant, Z. P. and Jirásek, M. (2002). Nonlocal integral formulations of plasticity and damage: survey of progress. *Journal of Engineering Mechanics*, 128(11):1119–1149.

Burr, A., Hild, F., and Leckie, F. (1995). Micro-mechanics and continuum damage mechanics. *Archive of applied mechanics*, 65(7):437–456.

Camus, G. (2000). Modelling of the mechanical behavior and damage processes of fibrous ceramic matrix composites: application to a 2-d sic/sic. *International Journal of solids and Structures*, 37(6):919–942.

DeRienzo, J. M. (2013). Biaxial (tension-torsion) testing of an oxide/oxide ceramic matrix composite. Master's thesis, Air Force Institute of Technology, Ohio.

Gasser, A., Ladevèze, P., and Pérès, P. (1998). Damage modelling for a laminated ceramic composite. *Materials Science and Engineering A*, 250:249–255.

Genin, G. M. and Hutchinson, J. W. (1997). Composite laminates in plane stress: constitutive modeling and stress redistribution due to matrix cracking. *Journal of the American Ceramic Society*, 80(5):1245–1255.

Hilburn, S. R. (2014). Experimental investigation of mechanical behavior of an oxide/oxide ceramic composite in interlaminar shear and under combined tension-torsion loading. Master's thesis, Air Force Institute of Technology, Ohio.

Hochard, C., Aubourg, P.-A., and Charles, J.-P. (2001). Modelling of the mechanical behaviour of woven-fabric cfrp laminates up to failure. *Composites Science and Technology*, 61(2):221–230.

Ladeveze, P. and LeDantec, E. (1992). Damage modelling of the elementary ply for laminated composites. *Composites Science and Technology*, 43(3):257–267.

Lemaitre, J. and Chaboche, J.-L. (1994). *Mechanics of solid materials*. Cambridge university press.

Lene, F. and Leguillon, D. (1982). Homogenized constitutive law for a partially cohesive composite material. *International Journal of Solids and Structures*, 18(5):443–458.

Sally, O., Julien, C., Laurin, F., Desmorat, R., and Bouillon, F. (2018). Fatigue lifetime modeling of oxide/oxide composites. *Procedia engineering*, 213:797–803.

Siron, O., Pailhes, J., and Lamon, J. (1999). Modelling of the stress/strain behaviour of a carbon/carbon composite with a 2.5 dimensional fibre architecture under tensile and shear loads at room temperature. *Composites science and technology*, 59(1):1–12.